Nanoscale Horizons

ROYAL SOCIETY OF CHEMISTRY

COMMUNICATION

View Article Online
View Journal | View Issue

Cite this: *Nanoscale Horiz.*, 2023, 8, 1686

Received 10th July 2023,
Accepted 1st September 2023

DOI: 10.1039/d3nh00282a

rsc.li/nanoscale-horizons

Quantum-sized topological insulators/semimetals enable ultrahigh and broadband saturable absorption†

Zhexue Chen,[ab] Xinyu Sui,[bc] Zhangqiang Li,[ab] Yueqi Li,[ab] Xinfeng Liu [bc] and Yong Zhang *[ab]

Two-dimensional topological insulators/semimetals have recently attracted much attention. However, quantum-sized topological insulators/semimetals with intrinsic characteristics have never been reported before. Herein, we report the high-yield production of topological insulator (*i.e.*, Bi_2Se_3 and Sb_2Te_3) and semimetal (*i.e.*, TiS_2) quantum sheets (QSs) with monolayer structures and sub-4 nm lateral sizes. Both linear and nonlinear optical performances of the QSs are investigated. The QS dispersions present remarkable photoluminescence with excitation wavelength-, concentration-, and solvent-dependence. The solution-processed QSs-poly(methyl methacrylate) (PMMA) hybrid thin films demonstrate exceptional nonlinear saturation absorption (NSA). Particularly, Bi_2Se_3 QSs-PMMA enables record-high NSA performance with a broadband feature. Specifically, the (absolute) modulation depths up to 71.6 and 72.4% and saturation intensities down to 1.52 and 0.49 MW cm^{-2} are achieved at 532 and 800 nm, respectively. Such a phenomenal NSA performance would greatly facilitate their applications in mode-locked lasers and related fields.

New concepts

Topological insulators and semimetals are important classes of 2D materials. Their quantum sheets (QSs) can be treated as extremely quantum-sized topological insulators/semimetals, whose production is highly desired but is far from satisfactory. We herein report the high-yield (>12 wt%) production of topological insulator (*i.e.*, Bi_2Se_3 and Sb_2Te_3) and semimetal (*i.e.*, TiS_2) QSs with monolayer structures and sub-4 nm lateral sizes. The QSs-poly(methyl methacrylate) (PMMA) hybrid thin films demonstrate exceptional nonlinear saturation absorption (NSA). Ultrahigh nonlinear response (72.4 and 68.4%) and ultralow power excitation (0.49 and 0.80 MW cm^{-2}) are simultaneously achieved in both Bi_2Se_3 QSs-PMMA and TiS_2 QSs-PMMA. Such phenomenal NSA performances in quantum-sized topological insulators/semimetals would greatly facilitate their applications in mode-locked lasers and related fields.

1. Introduction

Two-dimensional (2D) materials have attracted much interest over the past decade due to their fascinating structures and properties.[1,2] Topological insulators (*e.g.*, Bi_2Se_3, Bi_2Te_3, and Sb_2Te_3) and semimetals (*e.g.*, TiS_2 and $TiSe_2$) are important classes of 2D materials, which have emerged as the new frontiers of materials science.[3,4] Both topological insulators and semimetals possess extraordinary properties. The former features a gapless metallic state on their surfaces/edges and insulator characteristics in the bulk,[5] while the latter is characterized by bulk Dirac or Weyl fermions and nontrivial topological surface/edge states.[6] Such unique materials have been widely applied in various fields such as quantum physics,[7] spintronics and magnetoelectronics.[3,6] Compared with bulk layered materials and conventional 2D materials, extremely quantum-sized 2D materials (*e.g.*, 2D quantum sheets (QSs)) demonstrate remarkable performances because of their (both in-plane and out-of-plane) quantum confinement and prominent edge effects.[8] The production of 2D QSs of topological insulators and semimetals is highly desired but far from satisfactory. Fortunately, we have recently developed a general strategy towards the production of 2D QSs and zero-dimensional quantum dots (0D QDs) from their bulk materials.[8–13] However, whether the strategy could be applied for topological insulator and semimetal QS production has never been testified.

Nonlinear optical (NLO) response is the key factor for the evaluation of NLO materials. As a typical third-order NLO effect,

[a] *CAS Key Laboratory of Nanosystem and Hierarchical Fabrication, CAS Center for Excellence in Nanoscience, National Center for Nanoscience and Technology, Beijing 100190, P. R. China. E-mail: zhangyong@nanoctr.cn*
[b] *University of Chinese Academy of Sciences, Beijing 100049, P. R. China*
[c] *CAS Key Laboratory of Standardization and Measurement for Nanotechnology, CAS Center for Excellence in Nanoscience, National Center for Nanoscience and Technology, Beijing 100190, P. R. China*

† Electronic supplementary information (ESI) available. See DOI: https://doi.org/10.1039/d3nh00282a

nonlinear saturation absorption (NSA) has attracted growing attention due to their applications in mode-locked lasers and related fields.[14] 2D materials have shown their great potential in NSA by having a deep modulation depth and low saturation intensity.[15] Recently, quantum-sized materials have demonstrated exciting NSA performances.[8–13] Meanwhile, topological insulators and semimetals are interesting candidates for NSA thanks to their unique electronic structures.[16,17] Therefore, quantum-sized topological insulators and semimetals could be very promising in terms of NSA performances.

Herein, we report the successful production of topological insulator (*i.e.*, Bi_2Se_3 and Sb_2Te_3) and semimetal (*i.e.*, TiS_2) QSs directly from their bulk materials using an all-physical top-down method. The combination of silica-assisted ball-milling and sonication-assisted solvent exfoliation enabled the high-yield (>12 wt%) production of QSs with monolayer structures and extremely reduced lateral sizes (<4 nm). The as-produced QSs were structurally intrinsic, which could be determinative to their unique photoluminescence (PL) and NSA performances. The QS dispersions presented excitation wavelength-, concentration-, and solvent-dependent PL. The QSs-poly(methyl methacrylate) (PMMA) hybrid thin films demonstrated exceptional NSA performances. Particularly, the Bi_2Se_3 QSs-PMMA realized ultrahigh nonlinear response and ultralow power excitation at wavelengths of 532 and 800 nm.

2. Results and discussion

The production process of Bi_2Se_3 QSs is schematically illustrated in Fig. 1(a), where four sequential procedures: silica-assisted ball-milling, sonication-assisted solvent exfoliation,

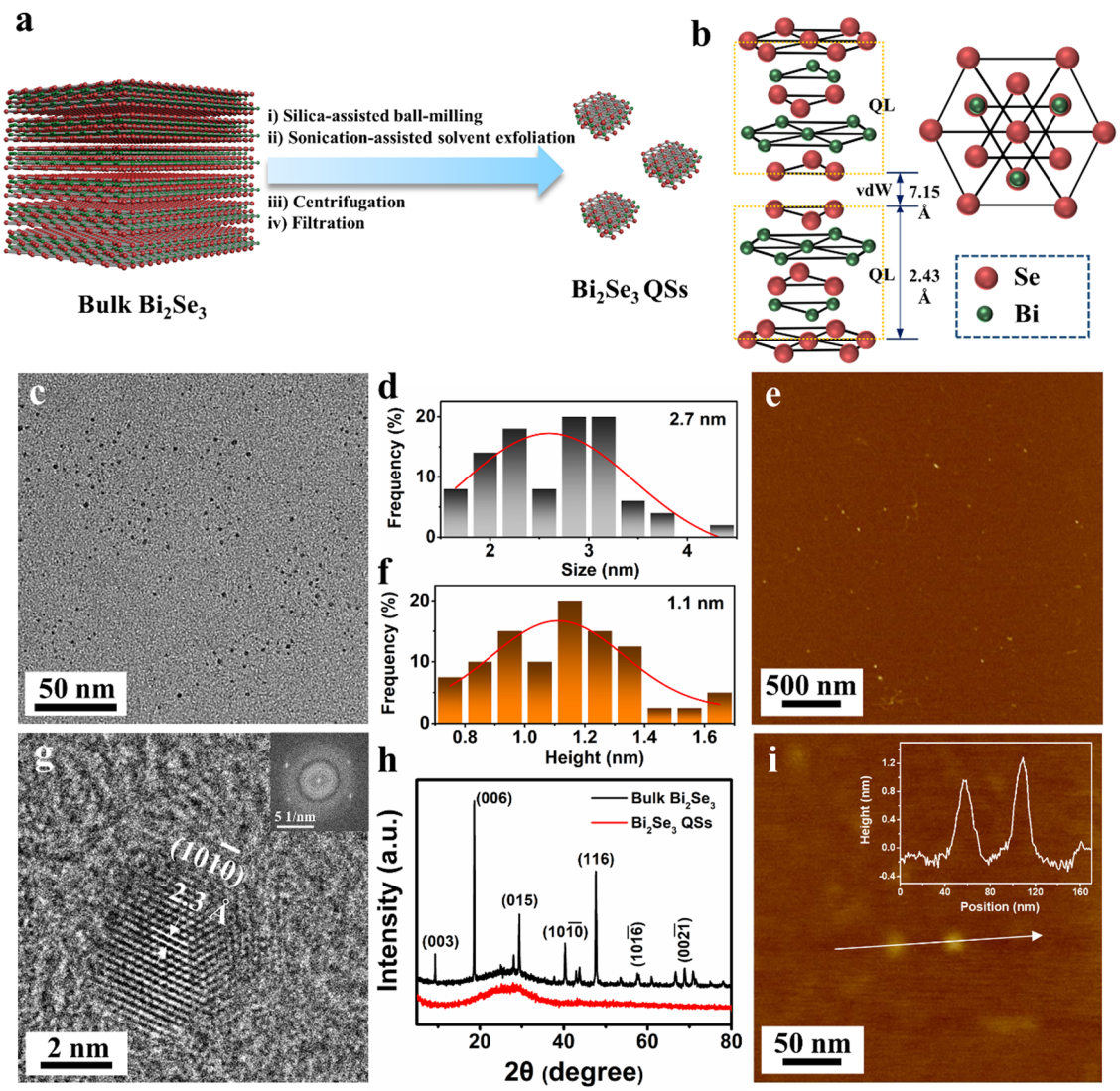

Fig. 1 Scalable production and microscopic characterization of the Bi_2Se_3 QSs. (a) Schematic illustration of the fabrication process. (b) Schematic diagram of the crystal structure. (c) TEM image. (d) Corresponding lateral size distribution. (e) AFM image. (f) Corresponding height distribution. (g) HRTEM image (inset showing the corresponding FFT pattern). (h) XRD patterns. Data for bulk Bi_2Se_3 are shown for comparison. (i) High-magnification AFM image (inset showing the corresponding height profile).

centrifugation and filtration were involved.[8] Sb_2Te_3 QSs and TiS_2 QSs were produced by the same method.[8] Excitingly, a single cycle of the production process enabled production of Bi_2Se_3 QSs, Sb_2Te_3 QSs, and TiS_2 QSs from their bulk materials (>50 μm, Fig. S1a–c, ESI†) with extremely high yield of 14.6, 12.1, 15.8 wt%, respectively, suggesting their great potential for future industrialization. No precipitation was observed for the QS redispersions (2 mg mL^{-1}) when standing still for 7 days under ambient conditions, indicating their long-term stability. Zeta potentials were measured to be −22.5, −27.6, −33.6 mV for Bi_2Se_3 QS, Sb_2Te_3 QS, and TiS_2 QS aqueous redispersions (0.1 mg mL^{-1}), respectively (Fig. S4, ESI†), supporting their satisfactory stability.

The crystal structure of the Bi_2Se_3 is schematically illustrated in Fig. 1(b), where the monolayer was constituted by five atomic layers. Multiple microscopic techniques were utilized for characterization of the Bi_2Se_3 QSs. Fig. 1 shows the corresponding transmission electron microscopy (TEM) and atomic force microscopy (AFM) images. The microscopic characterization of the Sb_2Te_3 QSs and TiS_2 QSs can be found in Fig. S2 and S3 (ESI†). From Fig. 1(c), the Bi_2Se_3 QSs with uniform shapes and sizes were obtained. The average lateral sizes of 2.7, 3.2, and 1.9 nm were derived for Bi_2Se_3 QSs, Sb_2Te_3 QSs, and TiS_2 QSs, respectively (Fig. 1(d) and Fig. S2, ESI†). Fig. 1(g) presents the high-resolution TEM (HRTEM) image and the corresponding fast Fourier transform (FFT) pattern of single Bi_2Se_3 QSs, indicating their single-crystalline structures. The lattice spacings of 0.23, 0.24, and 0.21 nm were revealed, corresponding to $(10\bar{1}\bar{0})$, $(10\bar{1}\bar{0})$, (102) crystal planes of Bi_2Se_3, Sb_2Te_3, and TiS_2, respectively (Fig. 1(g) and Fig. S2, ESI†). The average heights of 1.1, 1.2, and 0.7 nm were derived for Bi_2Se_3 QSs, Sb_2Te_3 QSs, and TiS_2 QSs, respectively (Fig. 1(e), (f) and Fig. S3, ESI†). The as-produced QSs were monolayers considering that the thicknesses of monolayer Bi_2Se_3, Sb_2Te_3, and TiS_2 were approximately 1, 1, and 0.6 nm, respectively.[18–20] Note that the individual height was acquired from the height profile of the single QS (Fig. 1(i)), which was the data source for the statistics in Fig. 1(f). Evidently, all the examined QSs were confirmed as quantum-sized monolayered structures.

Multiple spectroscopic techniques were utilized for further characterization of the as-produced QSs. Fig. 1(h) and Fig. S5 (ESI†) show the X-ray diffraction (XRD) patterns of the QSs. From Fig. 1(h), the characteristic peaks at 9.3, 18.6, 29.4, 40.3, 47.7, 57.6 and 68.9° correspond to (003), (006), (015), $(10\bar{1}\bar{0})$, (116), $(10\bar{1}\bar{6})$ and $(10\bar{2}\bar{1})$ crystal planes of Bi_2Se_3.[21] From Fig. S5a (ESI†), the characteristic peaks at 8.7, 17.4, 26.3, 28.2, 38.3, 44.6, 54.2, 63.2, and 74.8° were assigned to (003), (006), (009), (015), $(10\bar{1}\bar{0})$, $(10\bar{1}\bar{5})$, $(10\bar{1}\bar{8})$, $(10\bar{2}\bar{1})$ and $(10\bar{2}\bar{4})$ crystal planes of Sb_2Te_3.[22] From Fig. S5b (ESI†), the characteristic peaks at 15.5, 31.3, 34.2, 44.1, 47.8, 53.7, 57.6 and 65.5° were indexed to (001), (002), (101), (012), (003), (110), (103) and (004) crystal planes of 1T-TiS_2.[23] Compared with bulk layered materials, the as-produced QSs were identified with significantly reduced crystallinity and extremely enhanced edge states. The Raman spectra of the QSs are shown in Fig. 2(a), (d) and (g), where the insets schematically displayed the typical Raman vibrational modes. For Bi_2Se_3, as shown in Fig. 2(a), three characteristic peaks were observed in bulk and QSs. The peaks at 130.5 cm^{-1} were assigned to E_g^2 modes, whereas the peaks at 172.7 cm^{-1} corresponded to A_{1g}^2 modes.[24] Compared with bulk Bi_2Se_3, the Bi_2Se_3 QSs showed the E_g^2 modes and A_{1g}^2 modes with lower wavenumbers (*i.e.*, 128.8 and 172.2 cm^{-1}, respectively), which could be related to the relatively free states of vibrations in quantum-sized Bi_2Se_3.[24] For Sb_2Te_3, as shown in Fig. 2(d), the peaks at 121.6 cm^{-1} were assigned to E_u^2 modes, which could be infrared active.[25] The peaks at 139.3 cm^{-1} were attributed to the vibrational modes of the Te–Te bonds[26] and the peaks at 165.7 cm^{-1} were assigned to the A_{1g}^2 modes.[25] Compared with bulk Sb_2Te_3, the Sb_2Te_3 QSs presented greatly suppressed and notably blue-shifted (128.7 cm^{-1}) E_u^2 modes. Such unconventional blue-shift might be caused by the possible change of the topological structure/state (*e.g.*, electronic and vibrational properties) when transforming the bulk into QSs. On the one hand, the quantum confinement effects could alter the topological properties of the as-produced QSs. For instance, the time-reversal symmetry could be disrupted by external perturbations or confinement potentials, resulting in localization of electronic states.[27] On the other hand, the geometric anisotropy of the as-produced QSs could affect the spin–orbit coupling of its surface/edge state, thus modifying the bulk-edge correspondence and the value of the topological invariant.[28] The main reason for the blue-shift in Raman spectra could be attributed to the coupling between surface/edge states and bulk states, as well as the emerging localized states.[29,30] For TiS_2, as shown in Fig. 2(g), three characteristic peaks located at 149.2, 200.2, and 333.8 cm^{-1} were assigned to E_u, E_g, and A_{1g} modes, respectively, consistent with those reported previously.[31] Compared with bulk TiS_2, the TiS_2 QSs demonstrated quite weak E_u modes at 147.3 cm^{-1}. The above-mentioned weakening of Raman signals could be originated from the extremely reduced lateral sizes and layer numbers when tailoring bulk layered materials into their QSs. The constituent elements and chemical states of the as-produced QSs were analyzed by X-ray photoelectron spectroscopy (XPS). Fig. S6 (ESI†) shows the XPS full spectra, where no impurities (*e.g.*, Si from silica microspheres) were detected. Fig. 2(b), (c), (e), (f) and (h), (i) present the high-resolution XPS spectra, where both bulk and QSs were shown for comparison. For bulk Bi_2Se_3, as shown in Fig. 2(b) and (c), the two strong peaks at 158.2 and 163.5 eV corresponded to Bi $4f_{7/2}$ and Bi $4f_{5/2}$, while the two measured peaks at 53.6 and 54.4 eV were attributed to Se $3d_{5/2}$ and Se $3d_{3/2}$.[32] For Bi_2Se_3 QSs, the Bi 4f peaks (159.7 eV for Bi $4f_{7/2}$ and 165.0 eV for Bi $4f_{5/2}$) and Se 3d peaks (55.2 eV for Se $3d_{5/2}$ and 56.3 eV for Se $3d_{3/2}$) all shifted towards higher binding energy by 1.5–1.9 eV. As reported previously,[10] the extreme exposure of edge lattices/atoms in MoS_2 QSs would result in the XPS peak shifting towards lower binding energy. Therefore, the as-observed opposite shifting of the XPS peaks could be driven by the possible change of the topological structure/state in Bi_2Se_3 QSs. Similar trends were found in Sb_2Te_3 QSs and TiS_2 QSs. For bulk Sb_2Te_3, as shown in Fig. 2(e) and (f), the peaks at 528.6 and 538.0 eV were assigned

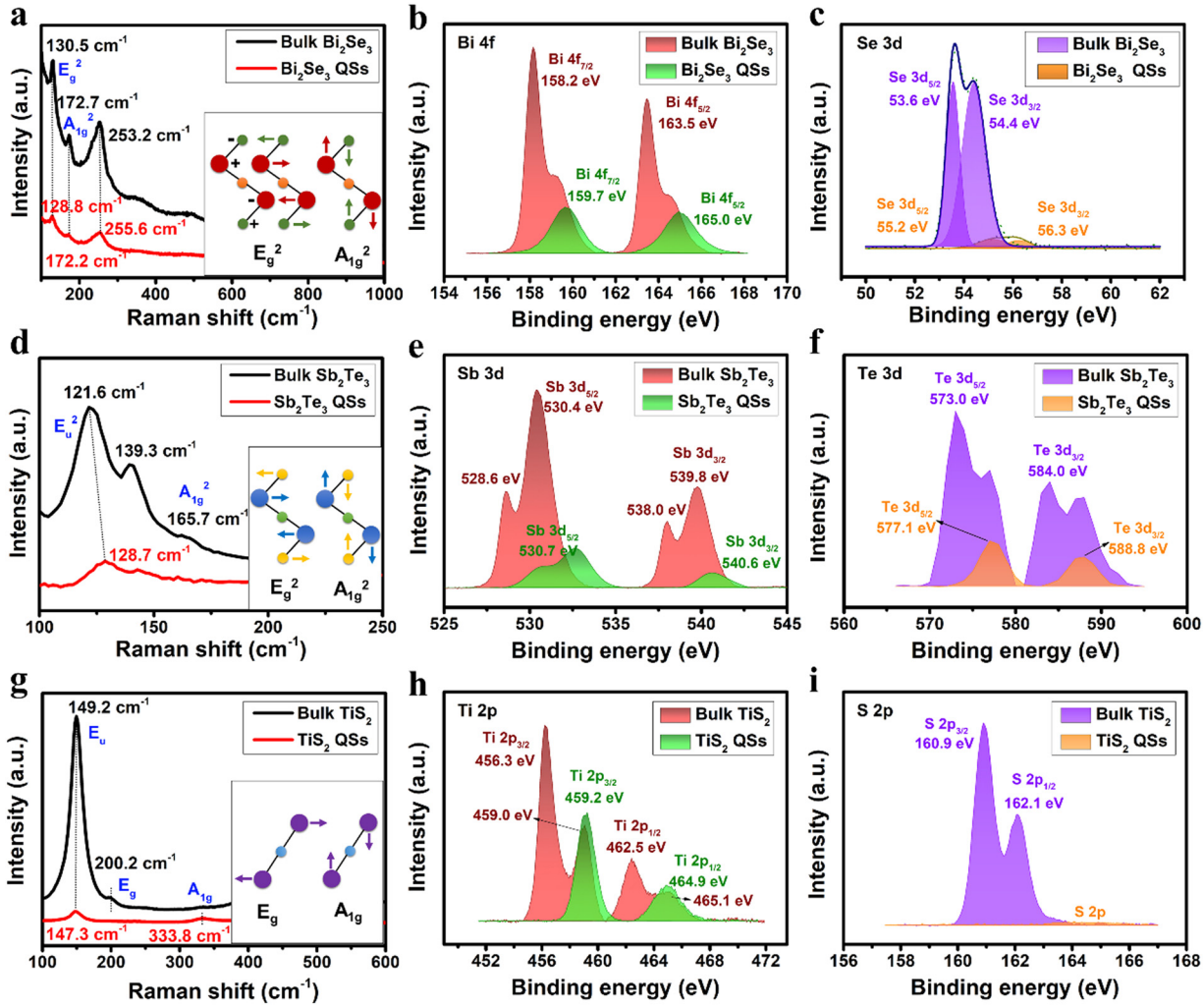

Fig. 2 Spectroscopic characterization of the as-produced QSs. Raman spectra of (a) Bi_2Se_3 QSs, (d) Sb_2Te_3 QSs, and (g) TiS_2 QSs. High-resolution XPS spectra of (b), (c) Bi_2Se_3 QSs, (e), (f) Sb_2Te_3 QSs, and (h), (i) TiS_2 QSs. Data for bulk materials are shown for comparison.

to Sb $3d_{5/2}$ and Sb $3d_{3/2}$, while the peaks at 573.0 and 584.0 eV were attributed to Te $3d_{5/2}$ and Te $3d_{3/2}$. The probable oxidation of bulk Sb_2Te_3 led to the occurrence of the peaks at 530.4 eV for the Sb $3d_{5/2}$ and 539.8 eV for the Sb $3d_{3/2}$.[33] For Sb_2Te_3 QSs, the Sb 3d peaks (530.7 eV for Sb $3d_{5/2}$ and 540.6 eV for Sb $3d_{3/2}$) and Te 3d peaks (577.1 eV for Te $3d_{5/2}$ and 588.8 eV for Te $3d_{3/2}$) shifted towards higher binding energy by 2.1–2.6 eV and 4.1–4.8 eV, respectively. For bulk TiS_2, as shown in Fig. 2(h) and (i), the peaks of Ti $2p_{3/2}$ and Ti $2p_{1/2}$ were located at 456.3 and 462.5 eV. The two strong peaks at 160.9 and 162.1 eV corresponded to S $2p_{3/2}$ and S $2p_{1/2}$, consistent with those of 1T-TiS_2.[23] For TiS_2 QSs, the Ti 2p peaks (459.2 eV for Ti $2p_{3/2}$ and 464.9 eV for Ti $2p_{1/2}$) shifted towards higher binding energy by 2.9 and 2.4 eV, respectively. The S 2p peaks shifted towards higher binding energy as well, although great suppression of the XPS signal was observed.

The optical properties of the as-produced QSs were investigated, as shown in Fig. 3 and Fig. S7–S11 (ESI†). Fig. 3(a)–(c) present the excitation wavelength-, concentration-, and solvent-dependent PL behavior of the Bi_2Se_3 QS dispersions. A similar phenomenon could be found in the Sb_2Te_3 and TiS_2 QS dispersions (Fig. S8–S10, ESI†). From Fig. 3(a), the PL intensity reached the maximum at the excitation wavelength of 360 nm for the Bi_2Se_3 QS dispersions. Such excitation wavelength-dependent PL behavior could be attributed to the size/thickness heterogeneity of the 2D QSs.[8] Fig. 3(b) shows the concentration-dependent PL behavior of the Bi_2Se_3 QS dispersions. The PL intensity was progressively enhanced with the concentration from 0.001 to 0.025 mg mL^{-1} because of the increase of the PL emitters. However, the PL intensity started to decrease with the concentration from 0.025 to 1 mg mL^{-1}, which could be ascribed to the aggregation-caused quenching (ACQ) mechanism.[8,34–36] Fig. 3(c) presents the solvent-dependent PL behavior of the Bi_2Se_3 QS dispersions. The PL intensity of the QS dispersions in varying solvents showed remarkable difference, which could be determined by QS-solvent (direct) interactions.[8,37,38] The PL lifetimes and quantum yields of the QSs were measured, as shown in Fig. 3(d) and Fig. S11 (ESI†). The PL lifetimes of Bi_2Se_3, Sb_2Te_3, and TiS_2 QSs were measured to be approximately 6.6, 7.0, and 3.1 ns, respectively. The

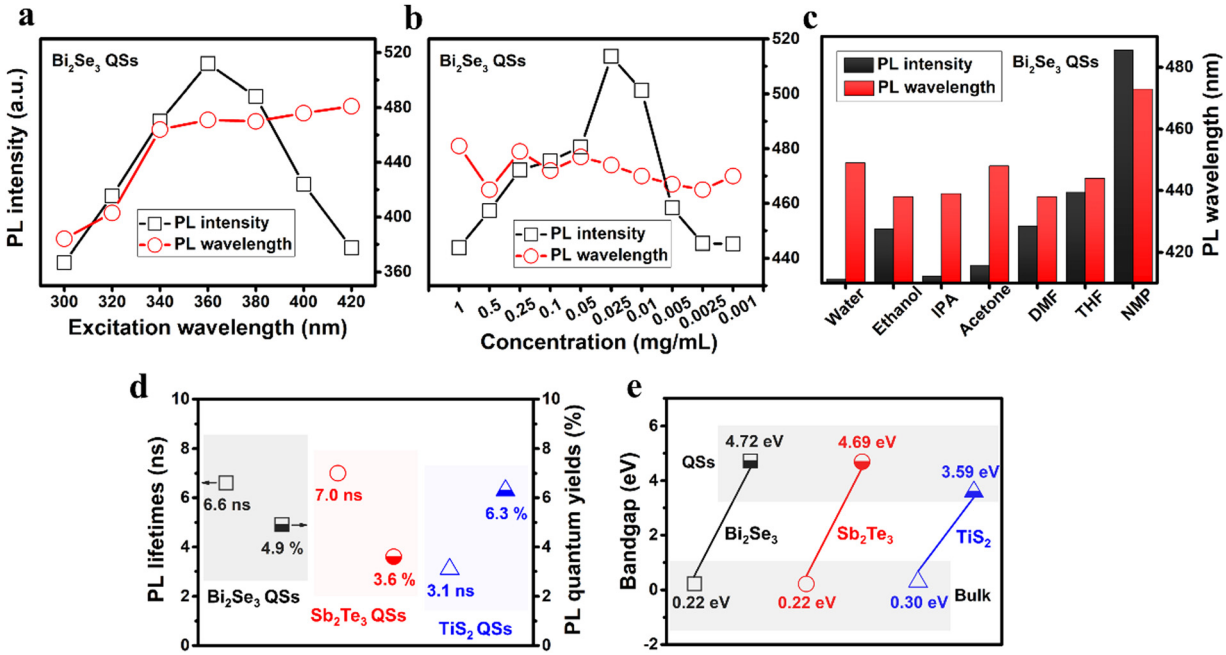

Fig. 3 Photoluminescence of the QS dispersions. (a) Excitation wavelength-dependent PL behavior. (b) Concentration-dependent PL behavior. (c) Solvent-dependent PL behavior. (d) PL lifetimes and quantum yields. (e) Optical bandgap-modulation by size-reduction.

absolute quantum yields were measured to be 4.9, 3.6, and 6.3% for the Bi_2Se_3, Sb_2Te_3, and TiS_2 QSs at the wavelength of 360, 360 and 380 nm, respectively. It should be noted that all the examined QSs exhibited blue PL, which could be determined by their bandgaps. The optical bandgaps were derived from the UV-vis absorption spectra, as shown in Fig. S7 (ESI†). Fig. 3(e) compares the optical bandgaps between bulk and QSs. For Bi_2Se_3, Sb_2Te_3, and TiS_2, with the sizes down to 2.7, 3.2, and 1.9 nm, the bandgaps increased to 4.72, 4.69, and 3.59 eV, much larger than those (*e.g.*, 0.22, 0.22, 0.30 eV) of bulk materials.[39–41] The as-produced QSs with extremely reduced thickness and lateral size would cause strong (out-of-plane and in-plane) quantum confinement effects, resulting in significant broadening of the optical bandgaps.[42,43] The bandgaps matched well with the blue emission of the QSs. Such (significant) bandgap-widening by (extreme) size-reduction would facilitate the practical applications of the topological insulators and semimetals.

Not only linear but also nonlinear optical performances of the as-produced QSs were explored. Fig. 4(a) shows the schematic setup for the NSA measurements. The laser pulse with wavelengths of 532 and 800 nm, duration of 100 fs, and repetition rate of 1 kHz was incident on an aperture of diameter 4 mm. Fig. S12a (ESI†) presents the photographs of the pure PMMA and QSs-PMMA thin films (with the thickness of 120 μm and the edge length of 1 cm). The QSs-PMMA thin films with the fixed loading content of 0.1 wt% demonstrated slightly lower transparency than that of the pure PMMA, further confirmed by UV-vis absorption spectroscopy (Fig. S12b, ESI†). Such high transparency would be the basic requirement for future applications. Note that there was no detectable aggregation/orientation of the QSs in the hybrid thin films, which was determined by the thermodynamic stability of such dispersions.[8] The NSA curves of the QSs-PMMA thin films are shown in Fig. S12c, d and S13 (ESI†). The normalized NSA curves (Fig. S13a and b, ESI†) were well fitted by the following formula: $\alpha^*(I) = \alpha_S^*/(1 + I/I_s) + \alpha_{NS}^*$[44] where $\alpha^*(I)$ is the absorption coefficient, α_S^* and α_{NS}^* are the saturable and non-saturable absorption components, I is the peak intensity (or power density) of the incident pulsed laser, and I_s is the saturation intensity defined as the optical intensity required in a steady state to reduce the absorption to half of its unbleached value. Fig. 4(b) summarizes the as-acquired NSA performances of the Bi_2Se_3, Sb_2Te_3, and TiS_2 QSs-PMMA thin films. From Fig. 4(b), unprecedented NSA performances were achieved in the QSs-PMMA thin films at wavelengths of both 532 and 800 nm. At 532 nm, the absolute modulation depths of 71.6, 45.1, and 43.6% as well as the saturation intensities of 1.52, 0.82, and 1.53 MW cm^{-2} (*i.e.*, 152, 82, and 153 nJ cm^{-2}) were derived for the Bi_2Se_3 QSs-PMMA, Sb_2Te_3 QSs-PMMA, and TiS_2 QSs-PMMA, respectively. At 800 nm, the absolute modulation depths of 72.4, 55.2, and 68.4% as well as the saturation intensities of 0.49, 0.34, and 0.80 MW cm^{-2} (*i.e.*, 49, 34, and 80 nJ cm^{-2}) were achieved for the Bi_2Se_3 QSs-PMMA, Sb_2Te_3 QSs-PMMA, and TiS_2 QSs-PMMA, respectively. Note that the Bi_2Se_3 QSs-PMMA retained extremely high NSA performances in the visible region, while the Sb_2Te_3 QSs-PMMA and TiS_2 QSs-PMMA demonstrated wavelength-dependent NSA performances. In addition, the TiS_2 QSs-PMMA showed comparable NSA performances to those of the Bi_2Se_3 QSs-PMMA at 800 nm, indicating the great potential in both topological insulators and semimetals. Besides the absolute modulation depths and

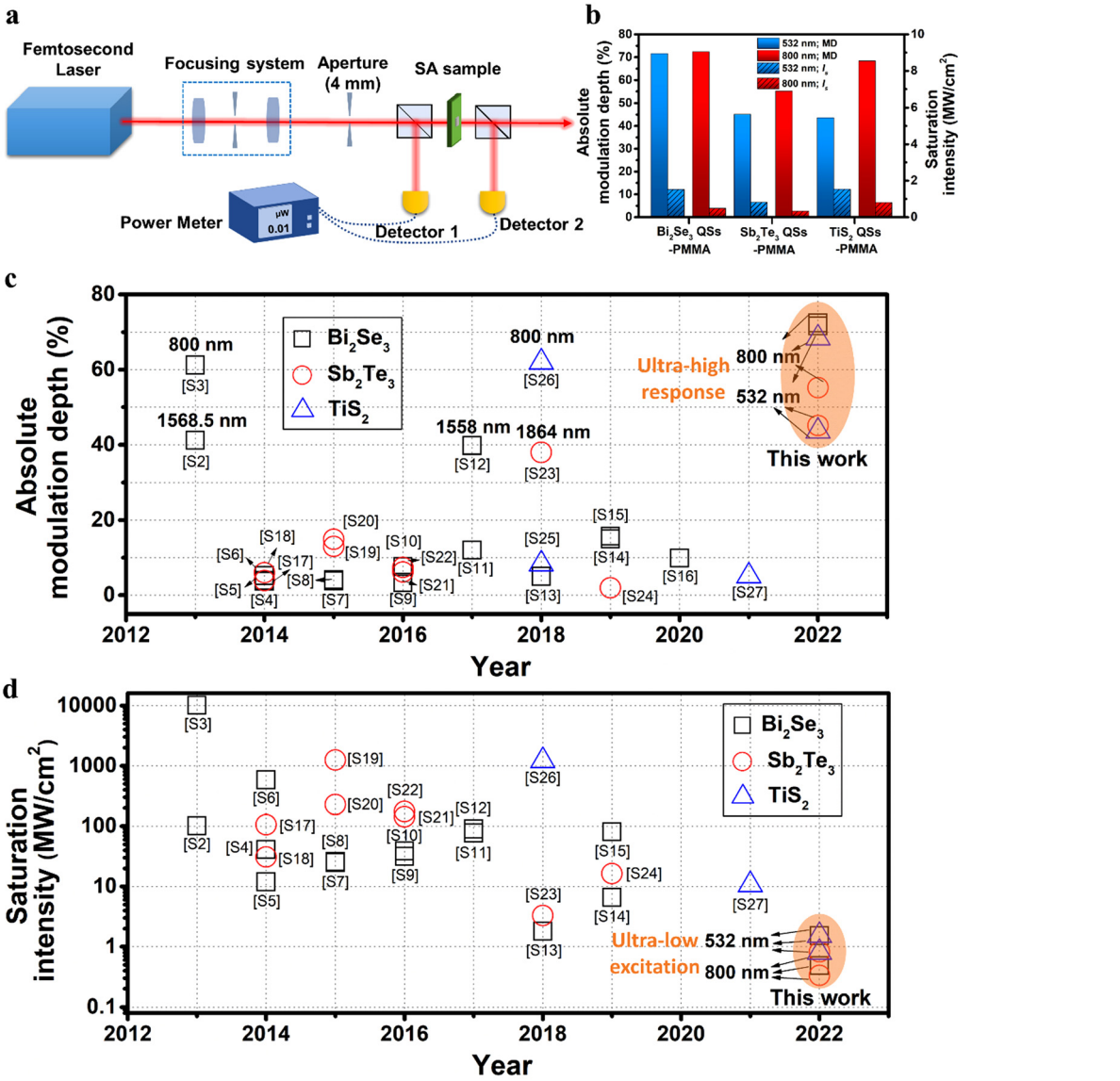

Fig. 4 NLO performances of the QS solid thin films. (a) Schematic setup of the NSA measurement. (b) Plots of the absolute modulation depth and saturation intensity. (c) and (d) NSA performance comparison in topological insulators/semimetals. The references (S2–S27) are listed in Table S1 and the ESI.†

saturation intensities, the relative modulation depths (*i.e.*, α_S^*) and nonsaturable losses (*i.e.*, α_{NS}^*) were derived, as shown in Fig. S13 (ESI†). All the examined QSs presented high α_S^* and satisfactory α_{NS}^*. Particularly, the Bi_2Se_3 QSs-PMMA demonstrated ultrahigh α_S^* of 95.9% and extremely low α_{NS}^* of 4.1%, further supporting its extraordinary NSA performances. Table S1 (ESI†) lists the NSA performances of the as-produced QSs and the topological insulators/semimetals from other works. Based on Table S1 (ESI†), the complete comparison of their NSA performances (*i.e.*, the absolute modulation depths and saturation intensities) was accomplished, as shown in Fig. 4(c) and (d). Excitingly, ultrahigh nonlinear response and ultralow power excitation were simultaneously achieved in the as-produced QSs. Meanwhile, the Bi_2Se_3 QSs-PMMA demonstrated record-high absolute modulation depth (72.4% at 800 nm), which had never been achieved before (not limited to topological insulators/semimetals). Such extraordinary NSA performances of the as-fabricated QSs-PMMA thin films could originate from three aspects: (1) the inherent characteristics of the material; (2) intrinsic edge effects; and (3) quantum confinement effect. Firstly, topological insulator/semimetal were a novel state of quantum matter with an insulating bulk state and gapless surface/edge states.[45,46] The unique electronic structure at the surface/edge states of the topological insulator/semimetal made it different from the traditional saturable absorbers (such as graphene, hexagonal boron nitride, transition metal dichalcogenides, In_2X_3(X = S, Se, Te), MXene) thus exhibited higher NSA performances.[8,9,47,48] Therefore, the inherent characteristics of topological insulator/semimetal played an important role in the NSA performances. Secondly,

the as-produced QSs possessed entirely exposed edges, maximizing their intrinsic edge effects (nonequilibrium situation (*e.g.*, broken lattices, unsaturated/dangling bonds, dynamic changes, *etc.*) and asymmetric environment). The lattice at the surfaces/edges would dominate compared with their internal lattice in the as-produced QSs. The key roles of the rich surface/edge electronic states on the NSA performances included two aspects: (1) the unique density of states leaded to a strong overlap between the electronic wavefunctions and incident photons, resulting in an enhanced light–matter interaction. Such interaction facilitated the absorption of the incident light; and (2) the surface/edge electronic states of the as-produced QSs were topologically protected, indicating that they were robust against disorders and perturbations. The robustness of the surface/edge states ensured their effective nonlinear saturation absorption. Hence, the surface/edge (free, nonequilibrium) electronic states played a significant role in their absorption of photons.[49] Thirdly, the extreme size-reduction in the QSs would induce (both in-plane and out-of-plane) quantum confinement effects. Such effects would change the electronic structure, exciton properties and density of states of the as-produced QSs, directly affecting the changes of its nonlinear absorption coefficient, saturation intensity and excited state dynamics, resulting in ultrahigh saturable absorption.[50–52] Evidently, the combination of the inherent characteristics of the material, quantum confinement and intrinsic edge effects could be determinative to their phenomenal NSA performances of the quantum-sized topological insulators and semimetals.

3. Conclusions

In summary, quantum-sized topological insulators/semimetals (*i.e.*, Bi_2Se_3 QSs, Sb_2Te_3 QSs, and TiS_2 QSs) were produced *via* an all-physical top-down method. The as-produced QSs were monolayers with intrinsic characteristics, which could be determinative to their extraordinary performances. The highly stable QS dispersions presented excitation wavelength-, concentration-, and solvent-dependent PL. The highly transparent QSs-PMMA thin films demonstrated broadband NSA in the visible. Ultrahigh nonlinear response (72.4 and 68.4%) and ultralow power excitation (0.49 and 0.80 MW cm^{-2}) were simultaneously achieved in both Bi_2Se_3 QSs-PMMA and TiS_2 QSs-PMMA. Compared with TiS_2 QSs-PMMA, Bi_2Se_3 QSs-PMMA maintained extremely high NSA performance at varying (laser) wavelength (532 and 800 nm). Such a highly desired broadband feature in quantum-sized topological insulators would undoubtedly facilitate their applications in mode-locked lasers and related fields.

Author contributions

Z. C. performed the experiments and characterization studies. Y. Z. supervised the research project. Y. Z. and Z. C. analyzed the data and wrote the manuscript. Z. L. and Y. L. helped with the spectroscopic characterization. X. S. and X. L. performed the nonlinear optical characterization.

Conflicts of interest

The authors declare no conflict of interest.

Acknowledgements

This work was supported by the National Natural Science Foundation of China (no. 52073070, 21673054, 11874130, and 22073022), the Strategic Priority Research Program of Chinese Academy of Sciences (no. XDB36000000), the National Key R&D Program of China (no. 2018YFA0703700), and the DNL Cooperation Fund CAS (DNL202016).

References

1 K. S. Novoselov, A. K. Geim, S. V. Morozov, D. Jiang, Y. Zhang, S. V. Dubonos, I. V. Grigorieva and A. A. Firsov, Electric field effect in atomically thin carbon films, *Science*, 2004, **306**, 666–669.
2 A. K. Geim, Graphene: Status and prospects, *Science*, 2009, **324**, 1530–1534.
3 Q. L. He, T. L. Hughes, N. P. Armitage, Y. Tokura and K. L. Wang, Topological spintronics and magnetoelectronics, *Nat. Mater.*, 2022, **21**, 15–23.
4 A. A. Burkov, Topological semimetals, *Nat. Mater.*, 2016, **15**, 1145–1148.
5 M. Z. Hasan and C. L. Kane, Colloquium: Topological insulators, *Rev. Mod. Phys.*, 2010, **82**, 3045–3067.
6 A. Wang, X. Ye, D. Yu and Z. Liao, Topological semimetal nanostructures: From properties to topotronics, *ACS Nano*, 2020, **14**, 3755–3778.
7 O. Breunig and Y. Ando, Opportunities in topological insulator devices, *Nat. Rev. Phys.*, 2022, **4**, 184–193.
8 Y. Xu, S. Chen, Z. Dou, Y. Ma, Y. Mi, W. Du, Y. Liu, J. Zhang, J. Chang, C. Liang, J. Zhou, H. Guo, P. Gao, X. Liu, Y. Che and Y. Zhang, Robust production of 2D quantum sheets from bulk layered materials, *Mater. Horiz.*, 2019, **6**, 1416–1424.
9 C. Han, Y. Zhang, P. Gao, S. Chen, X. Liu, Y. Mi, J. Zhang, Y. Ma, W. Jiang and J. Chang, High-yield production of MoS_2 and WS_2 quantum sheets from their bulk materials, *Nano Lett.*, 2017, **17**, 7767–7772.
10 C. Liang, X. Sui, A. Wang, J. Chang, W. Wang, Z. Chen, W. Jiang, Y. Ma, J. Zhang, X. Liu and Y. Zhang, Controlled production of MoS_2 full-scale nanosheets and their strong size effects, *Adv. Mater. Interfaces*, 2020, **7**, 2001130.
11 Y. Xu, J. Chang, C. Liang, X. Sui, Y. Ma, L. Song, W. Jiang, J. Zhou, H. Guo, X. Liu and Y. Zhang, Tailoring multi-walled carbon nanotubes into graphene quantum sheets, *ACS Appl. Mater. Interfaces*, 2020, **12**, 47784–47791.
12 Y. Xu, W. Wang, Z. Chen, X. Sui, A. Wang, C. Liang, J. Chang, Y. Ma, L. Song, W. Jiang, J. Zhou, X. Liu and Y. Zhang, A general strategy for semiconductor quantum dot production, *Nanoscale*, 2021, **13**, 8004–8011.
13 Z. Chen, W. Wang, X. Sui, K. Wang, J. Zhang, X. Liu and Y. Zhang, Quantum-sized silicon for enhanced photoluminescence and optical nonlinearity, *Mater. Chem. Front.*, 2021, **5**, 7817–7823.

14 V. V. Zubyuk, P. P. Vabishchevich, M. R. Shcherbakov, A. S. Shorokhov, A. N. Fedotova, S. Liu, G. Keeler, T. V. Dolgova, I. Staude, I. Brener and A. A. Fedyanin, Low-power absorption saturation in semiconductor metasurfaces, *ACS Photonics*, 2019, **6**, 2797–2806.
15 G. Wang, A. A. Baker-Murray and W. J. Blau, Saturable absorption in 2D nanomaterials and related photonic devices, *Laser Photonics Rev.*, 2019, **13**, 1800282.
16 X. Liu, Q. Guo and J. Qiu, Emerging low-dimensional materials for nonlinear optics and ultrafast photonics, *Adv. Mater.*, 2017, **29**, 1605886.
17 Y. Ge, Z. Zhu, Y. Xu, Y. Chen, S. Chen, Z. Liang, Y. Song, Y. Zou, H. Zeng, S. Xu, H. Zhang and D. Fan, Broadband nonlinear photoresponse of 2D TiS_2 for ultrashort pulse generation and all-optical thresholding devices, *Adv. Opt. Mater.*, 2018, **6**, 1701166.
18 A. I. Komonov, V. Y. Prinz, V. A. Seleznev, K. A. Kokh and V. N. Shlegel, Step-height standards based on the rapid formation of monolayer steps on the surface of layered crystals, *Appl. Surf. Sci.*, 2017, **410**, 1–7.
19 M. Xia, K. Ding, F. Rao, X. Li, L. Wu and Z. Song, Aluminum-centered tetrahedron-octahedron transition in advancing Al–Sb–Te phase change properties, *Sci. Rep.*, 2015, **5**, 8548.
20 Z. Gao, Q. Ji, P.-C. Shen, Y. Han, W. S. Leong, N. Mao, L. Zhou, C. Su, J. Niu, X. Ji, M. M. Goulamaly, D. A. Muller, Y. Li and J. Kong, *In situ*-generated volatile precursor for CVD growth of a semimetallic 2D dichalcogenide, *ACS Appl. Mater. Interfaces*, 2018, **10**, 34401–34408.
21 H. Lai, S. Jian, L. T. C. Tuyen, P. H. Le, C. Luo and J. Juang, Nanoindentation of Bi_2Se_3 thin films, *Micromachines*, 2018, **9**, 518.
22 B. Lv, S. Hu, W. Li, X. Di, L. Feng, J. Zhang, L. Wu, Y. Cai, B. Li and Z. Lei, Preparation and characterization of Sb_2Te_3 thin films by coevaporation, *Int. J. Photoenergy*, 2010, **2010**, 476589.
23 Y. Liu, C. Liang, J. Wu, T. Sharifi, H. Xu, Y. Nakanishi, Y. Yang, C. F. Woellne, A. Aliyan, A. A. Martí, B. Xie, R. Vajtai, W. Yang and P. M. Ajayan, Atomic layered titanium sulfide quantum dots as electrocatalysts for enhanced hydrogen evolution reaction, *Adv. Mater. Interfaces*, 2018, **5**, 1700895.
24 J. Zhang, Z. Peng, A. Soni, Y. Zhao, Y. Xiong, B. Peng, J. Wang, M. S. Dresselhaus and Q. Xiong, Raman spectroscopy of few-quintuple layer topological insulator Bi_2Se_3 nanoplatelets, *Nano Lett.*, 2011, **11**, 2407–2414.
25 K. Norimatsu, M. Hada, S. Yamamoto, T. Sasagawa, M. Kitajima, Y. Kayanuma and K. G. Nakamura, Dynamics of all the Raman-active coherent phonons in Sb_2Te_3 revealed *via* transient reflectivity, *J. Appl. Phys.*, 2015, **117**, 143102.
26 S. A. Nemov, V. D. Andreeva, Y. V. Ulashkevich, A. V. Povolotsky and A. A. Allahkhah, Specific features of the IR reflectance and Raman spectra of $Sb_2Te_{3-x}Se_x$ crystals, *Semiconductors*, 2018, **52**, 1317–1322.
27 M. S. Bahramy, P. D. C. King, A. de la Torre, J. Chang, M. Shi, L. Patthey, G. Balakrishnan, P. Hofmann, R. Arita, N. Nagaosa and F. Baumberger, Emergent quantum confinement at topological insulator surfaces, *Nat. Commun.*, 2012, **3**, 1159.
28 H. Kurebayashi, J. H. Garcia, S. Khan, J. Sinova and S. Roche, Magnetism, symmetry and spin transport in van der Waals layered systems, *Nat. Rev. Phys.*, 2022, **4**, 150–166.
29 H. H. Kung, M. Salehi, I. Boulares, A. F. Kemper, N. Koirala, M. Brahlek, P. Lošťák, C. Uher, R. Merlin, X. Wang, S. W. Cheong, S. Oh and G. Blumberg, Surface vibrational modes of the topological insulator Bi_2Se_3 observed by Raman spectroscopy, *Phys. Rev. B*, 2017, **95**, 245406.
30 H. Padmanabhan, M. Poore, P. K. Kim, N. Z. Koocher, V. A. Stoica, D. Puggioni, H. Wang, X. Shen, A. H. Reid, M. Gu, M. Wetherington, S. H. Lee, R. D. Schaller, Z. Mao, A. M. Lindenberg, X. Wang, J. M. Rondinelli, R. D. Averitt and V. Gopalan, Interlayer magnetophononic coupling in $MnBi_2Te_4$, *Nat. Commun.*, 2022, **13**, 1929.
31 X. Zhu, S. Chen, M. Zhang, L. Chen, Q. Wu, J. Zhao, Q. Jiang, Z. Zheng and H. Zhang, TiS_2-based saturable absorber for ultrafast fiber lasers, *Photonics Res.*, 2018, **6**, C44–C48.
32 C. Liu, H. Zhang, Z. Sun, K. Ding, J. Mao, Z. Shao and J. Jie, Topological insulator Bi_2Se_3 nanowire/Si heterostructure photodetectors with ultrahigh responsivity and broadband response, *J. Mater. Chem. C*, 2016, **4**, 5648–5655.
33 J. Schaumann, M. Loor, D. Ünal, A. Mudring, S. Heimann, U. Hagemann, S. Schulz, F. Maculewicz and G. Schierning, Improving the *zT* value of thermoelectrics by nanostructuring: tuning the nanoparticle morphology of Sb_2Te_3 by using ionic liquids, *Dalton Trans.*, 2017, **46**, 656–668.
34 Y. Hong, J. W. Y. Lam and B. Tang, Aggregation-induced emission: phenomenon, mechanism and applications, *Chem. Commun.*, 2009, 4332–4353.
35 W. Z. Yuan, P. Lu, S. Chen, J. W. Y. Lam, Z. Wang, Y. Liu, H. S. Kwok, Y. Ma and B. Z. Tang, Changing the behavior of chromophores from aggregation-caused quenching to aggregation-induced emission: Development of highly efficient light emitters in the solid state, *Adv. Mater.*, 2010, **22**, 2159–2163.
36 L. Cao, M. J. Meziani, S. Sahu and Y. P. Sun, Photoluminescence properties of graphene versus other carbon nanomaterials, *Acc. Chem. Res.*, 2013, **46**, 171–180.
37 C. Wang, L. Zhang, J. Wang, S. Su, X. Jin, P. An, B. Sun and Y. Luo, Ultra-thin two-dimensional nanosheets for in-situ NIR light-triggered fluorescence enhancement, *FlatChem*, 2020, **24**, 100193.
38 H. Jin, B. Baek, D. Kim, F. Wu, J. D. Batteas, J. Cheon and D. H. Son, Effects of direct solvent-quantum dot interaction on the optical properties of colloidal monolayer WS_2 quantum dots, *Nano Lett.*, 2017, **17**, 7471–7477.
39 G. Martinez, B. A. Piot, M. Hakl, M. Potemski, Y. S. Hor, A. Materna, S. G. Strzelecka, A. Hruban, O. Caha, J. Novák, A. Dubroka, Č. Drašar and M. Orlita, Determination of the energy band gap of Bi_2Se_3, *Sci. Rep.*, 2017, **7**, 6891.
40 A. Lawal, A. Shaari, R. Ahmed and N. Jarkoni, Sb_2Te_3 crystal a potential absorber material for broadband photodetector: A first-principles study, *Results Phys.*, 2017, **7**, 2302–2310.

41 C. Weng, Y. Luo, B. Wang, J. Shi, L. Gao, Z. Cao and G. Duan, Layer-dependent SERS enhancement of TiS_2 prepared by simple electrochemical intercalation, *J. Mater. Chem. C*, 2020, **8**, 14138–14145.
42 Z. X. Gan, L. Z. Liu, H. Y. Wu, Y. L. Hao, Y. Shan, X. L. Wu and P. K. Chu, Quantum confinement effects across two-dimensional planes in MoS_2 quantum dots, *Appl. Phys. Lett.*, 2015, **106**, 233113.
43 Y. Wang, Y. Liu, J. Zhang, J. Wu, H. Xu, X. Wen, X. Zhang, C. S. Tiwary, W. Yang, R. Vajtai, Y. Zhang, N. Chopra, I. N. Odeh, Y. Wu and P. M. Ajayan, Cryo-mediated exfoliation and fracturing of layered materials into 2D quantum dots, *Sci. Adv.*, 2017, **3**, e1701500.
44 Q. Bao, H. Zhang, Y. Wang, Z. Ni, Y. Yan, Z. Shen, K. P. Loh and D. Tang, Atomic-layer graphene as a saturable absorber for ultrafast pulsed lasers, *Adv. Funct. Mater.*, 2009, **19**, 3077–3083.
45 B. A. Bernevig, T. L. Hughes and S. C. Zhang, Quantum spin hall effect and topological phase transition in HgTe quantum wells, *Science*, 2006, **314**, 1757–1761.
46 J. E. Moore, The birth of topological insulators, *Nature*, 2010, **464**, 194–198.
47 W. Wang, Z. Chen, X. Sui, Y. Li, X. Liu and Y. Zhang, Phase/size dual controlled 2D semiconductor In_2X_3 (X = S, Se, Te) for saturable absorption modulation, *Nano Res.*, 2022, **15**, 5633–5639.
48 Z. Chen, X. Sui, Y. Li, X. Liu and Y. Zhang, Ti_3AlC_2 MAX and Ti_3C_2 MXene quantum sheets for record-high optical nonlinearity. J. Phys, *Chem. Lett.*, 2022, **13**, 3929–3936.
49 X. Zhang, J. Wang and S. Zhang, Topological insulators for high-performance terahertz to infrared applications, *Phys. Rev. B: Condens. Matter Mater. Phys.*, 2010, **82**, 245107.
50 Q. Gao, Y. Peng, T. Wang, C. Shen, C. Xia, J. Yang and Z. Wei, Quantum confinement effects on excitonic properties in the 2D vdW quantum system: The ZnO/WSe_2 case, *Adv. Photonics Res.*, 2021, **2**, 2000114.
51 S. Haldar, V. K. Dixit, G. Vashisht, S. K. Khamari, S. Porwal, T. K. Sharma and S. M. Oak, Effect of carrier confinement on effective mass of excitons and estimation of ultralow disorder in $Al_xGa_{1-x}As$/GaAs quantum wells by magneto-photoluminescence, *Sci. Rep.*, 2017, **7**, 4905.
52 N. P. Wilson, W. Yao, J. Shan and X. Xu, Excitons and emergent quantum phenomena in stacked 2D semiconductors, *Nature*, 2021, **599**, 383–392.

